BEILSTEIN

JOURNAL OF NANOTECHNOLOGY

BEILSTEIN JOURNAL OF NANOTECHNOLOGY

OPEN ACCESS PLATINUM

VOLUME NO. 8

2017

PAGES 1 - 2817

Table of Contents

JUMP TO

Select Article

Editorial Board Members

KEEP INFORMED

RSS Feed

Subscribe to our *Latest Articles* RSS Feed.

SUBSCRIBE

Follow the Beilstein-Institut

LinkedIn

Twitter: @BeilsteinInst

VOLUME NO. 8
2017
PAGES 1 - 2817

Table of Contents

Bio-inspired micro-to-nanoporous polymers with tunable stiffness

Julia Syurik, Ruth Schwaiger, Prerna Sudera, Stephan Weyand, Siegbert Johnsen, Gabriele Wiegand and Hendrik Hölscher

Full Research Paper | Published 21 Apr 2017

PDF Album Supp. Info

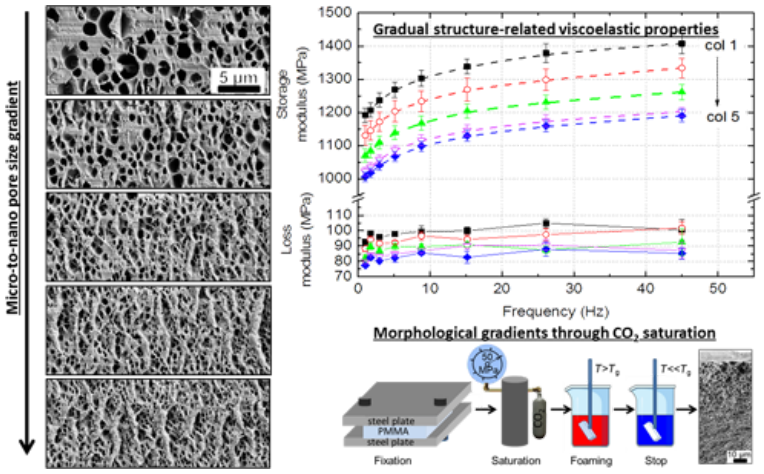

Beilstein J. Nanotechnol. **2017,** *8,* 906–914, doi:10.3762/bjnano.8.92

High photocatalytic activity of Fe_2O_3/TiO_2 nanocomposites prepared by photodeposition for degradation of 2,4-dichlorophenoxyacetic acid

Shu Chin Lee, Hendrik O. Lintang and Leny Yuliati

Full Research Paper **Published 24 Apr 2017**

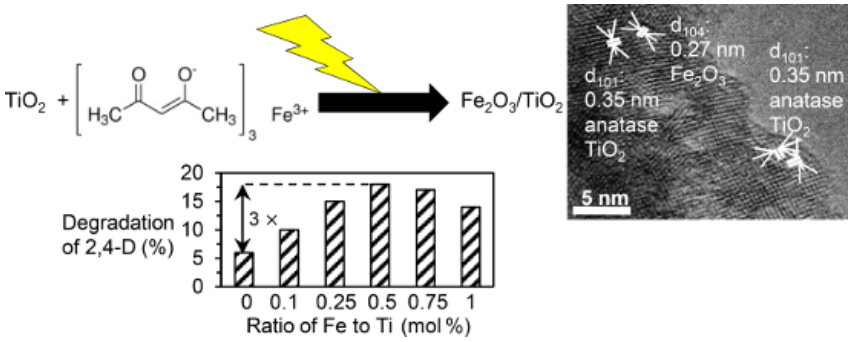

Beilstein J. Nanotechnol. **2017,** *8,* 915–926, doi:10.3762/bjnano.8.93

Energy-level alignment at interfaces between manganese phthalocyanine and C_{60}

Daniel Waas, Florian Rückerl, Martin Knupfer and Bernd Büchner

Full Research Paper **Published 25 Apr 2017**

PDF Album Supp. Info

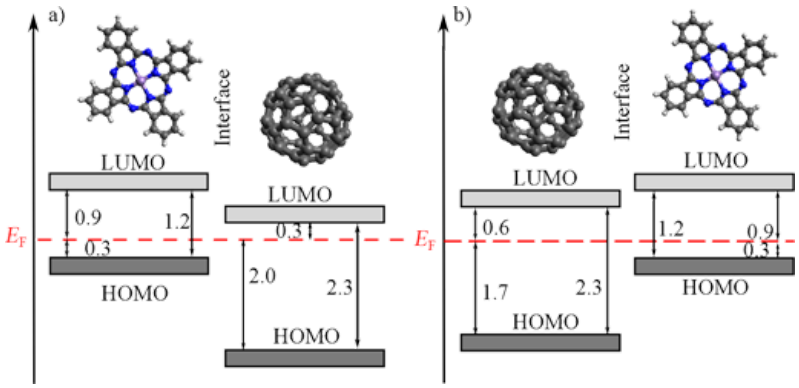

Beilstein J. Nanotechnol. **2017,** *8,* 927–932, doi:10.3762/bjnano.8.94

Vapor-phase-synthesized fluoroacrylate polymer thin films: thermal stability and structural properties

Paul Christian and Anna Maria Coclite

Full Research Paper | Published 26 Apr 2017

PDF Album Supp. Info

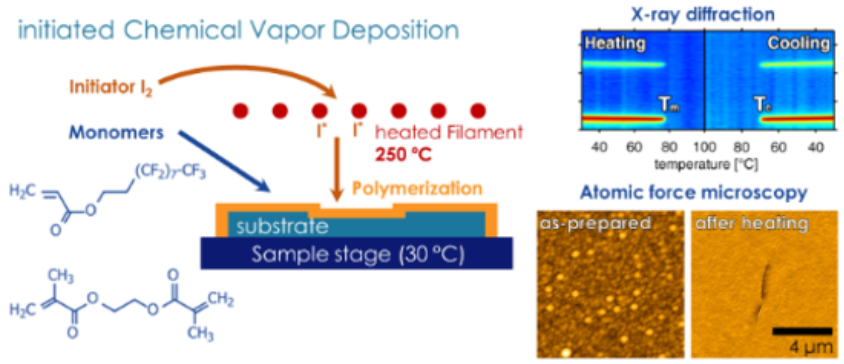

Beilstein J. Nanotechnol. **2017,** *8,* 933–942, doi:10.3762/bjnano.8.95

Tuning the spin coherence time of Cu(II)−(bis)oxamato and Cu(II)−(bis)oxamidato complexes by advanced ESR pulse protocols

Ruslan Zaripov, Evgeniya Vavilova, Iskander Khairuzhdinov, Kev Salikhov, Violeta Voronkova, Mohammad A. Abdulmalic, Francois E. Meva, Saddam Weheabby, Tobias Rüffer, Bernd Büchner and Vladislav Kataev

Full Research Paper | Published 27 Apr 2017

PDF Album

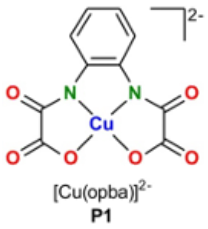

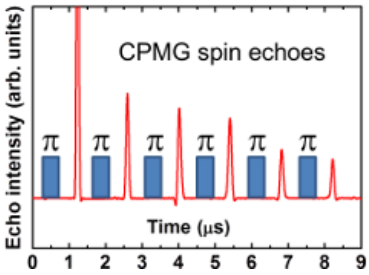

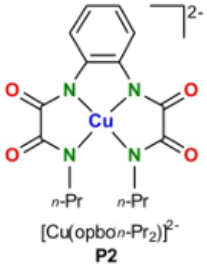

Beilstein J. Nanotechnol. **2017,** *8,* 943–955, doi:10.3762/bjnano.8.96

Near-field surface plasmon field enhancement induced by rippled surfaces

Mario D'Acunto, Francesco Fuso, Ruggero Micheletto, Makoto Naruse, Francesco Tantussi and Maria Allegrini

Full Research Paper | Published 28 Apr 2017

PDF Album Supp. Info

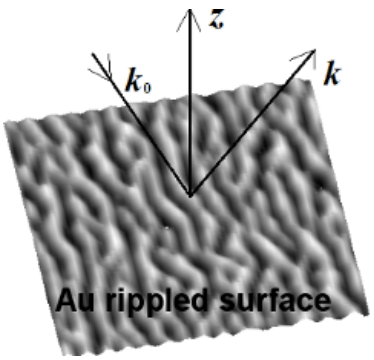

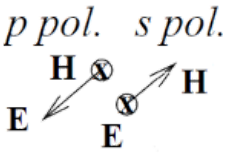

Beilstein J. Nanotechnol. **2017,** *8,* 956–967, doi:10.3762/bjnano.8.97

Scaling law to determine peak forces in tapping-mode AFM experiments on finite elastic soft matter systems

Horacio V. Guzman

Full Research Paper | Published 02 May 2017

PDF Album

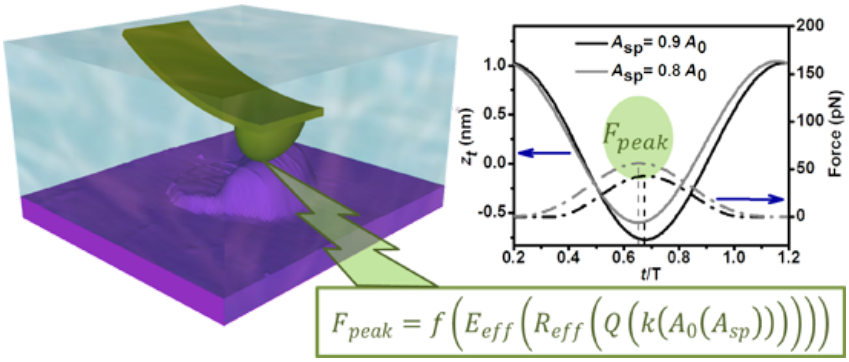

Beilstein J. Nanotechnol. **2017,** *8,* 968–974, doi:10.3762/bjnano.8.98

Nanoantenna-assisted plasmonic enhancement of IR absorption of vibrational modes of organic molecules

Alexander G. Milekhin, Olga Cherkasova, Sergei A. Kuznetsov, Ilya A. Milekhin, Ekatherina E. Rodyakina, Alexander V. Latyshev, Sreetama Banerjee, Georgeta Salvan and Dietrich R. T. Zahn

Full Research Paper | Published 03 May 2017

PDF Album

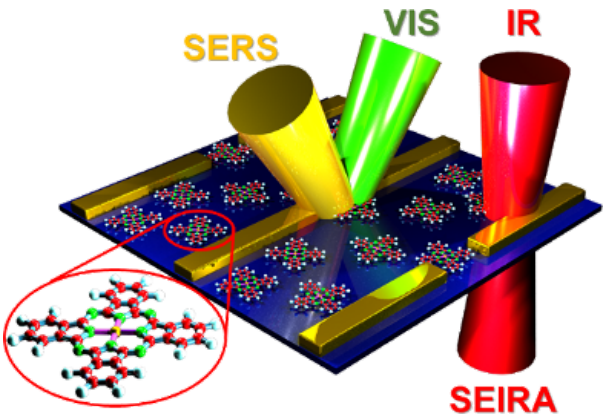

Beilstein J. Nanotechnol. **2017,** *8,* 975–981, doi:10.3762/bjnano.8.99

BTEX detection with composites of ethylenevinyl acetate and nanostructured carbon

Santa Stepina, Astrida Berzina, Gita Sakale and Maris Knite

Full Research Paper | Published 04 May 2017

PDF Album

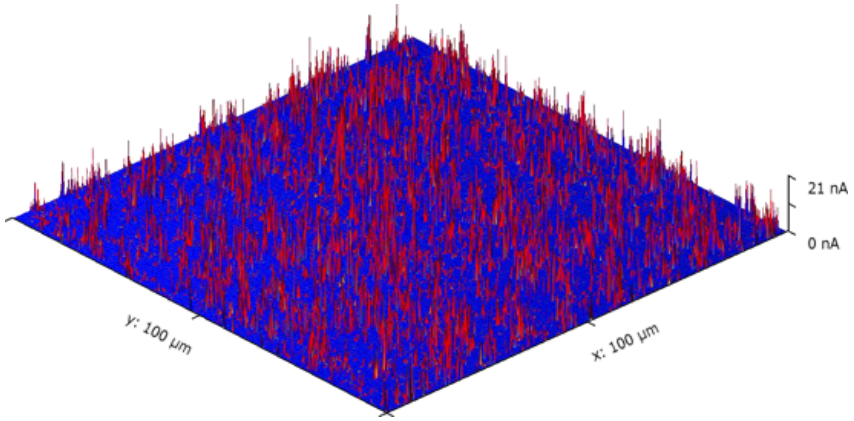

Beilstein J. Nanotechnol. **2017,** *8,* 982–988, doi:10.3762/bjnano.8.100

Needs and challenges for assessing the environmental impacts of engineered nanomaterials (ENMs)

Michelle Romero-Franco, Hilary A. Godwin, Muhammad Bilal and Yoram Cohen

Review | Published 05 May 2017

PDF Album Supp. Info

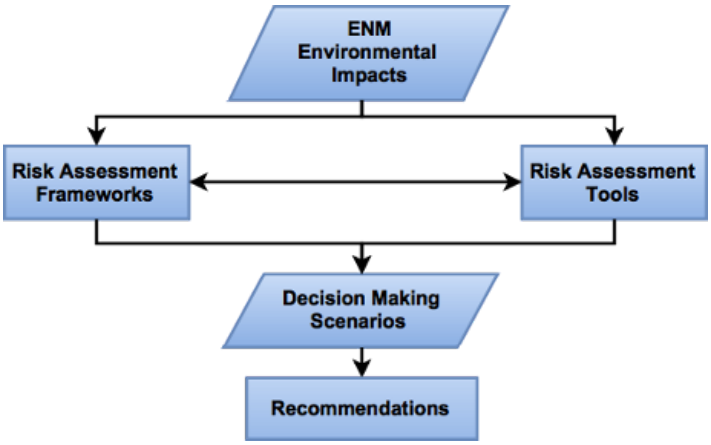

Beilstein J. Nanotechnol. **2017,** *8,* 989–1014, doi:10.3762/bjnano.8.101

CVD transfer-free graphene for sensing applications

Chiara Schiattarella, Sten Vollebregt, Tiziana Polichetti, Brigida Alfano, Ettore Massera, Maria Lucia Miglietta, Girolamo Di Francia and Pasqualina Maria Sarro

Full Research Paper | Published 08 May 2017

PDF Album

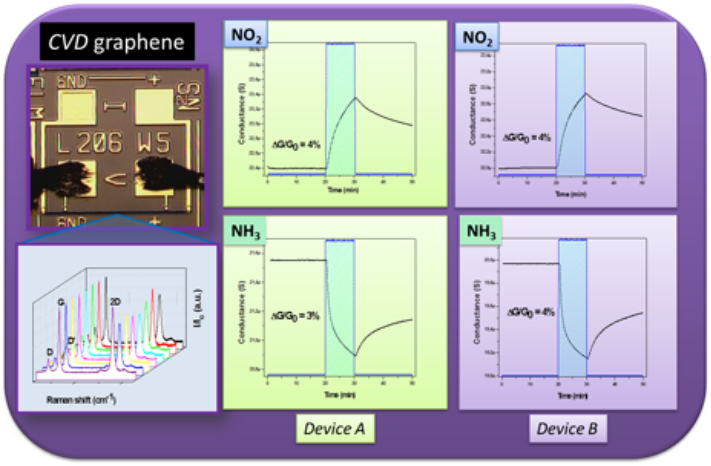

Beilstein J. Nanotechnol. **2017,** *8,* 1015–1022, doi:10.3762/bjnano.8.102

Study of the correlation between sensing performance and surface morphology of inkjet-printed aqueous graphene-based chemiresistors for NO_2 detection

F. Villani, C. Schiattarella, T. Polichetti, R. Di Capua, F. Loffredo, B. Alfano, M. L. Miglietta, E. Massera, L. Verdoliva and G. Di Francia

Full Research Paper | Published 09 May 2017

PDF Album Supp. Info

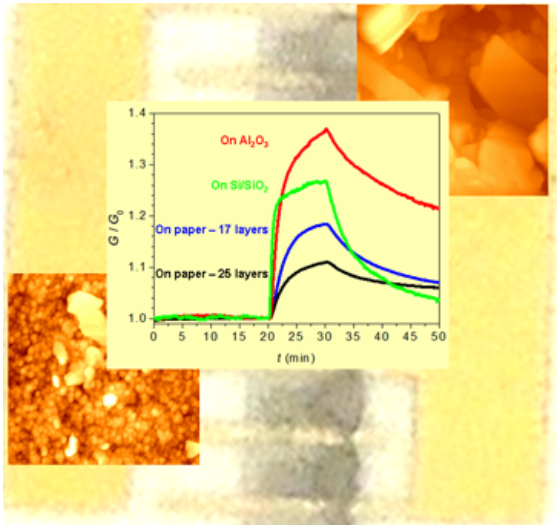

Beilstein J. Nanotechnol. **2017,** *8,* 1023–1031, doi:10.3762/bjnano.8.103

Structural properties and thermal stability of cobalt- and chromium-doped α-MnO_2 nanorods

Romana Cerc Korošec, Polona Umek, Alexandre Gloter, Jana Padežnik Gomilšek and Peter Bukovec

Full Research Paper **Published 10 May 2017**

PDF **Album**

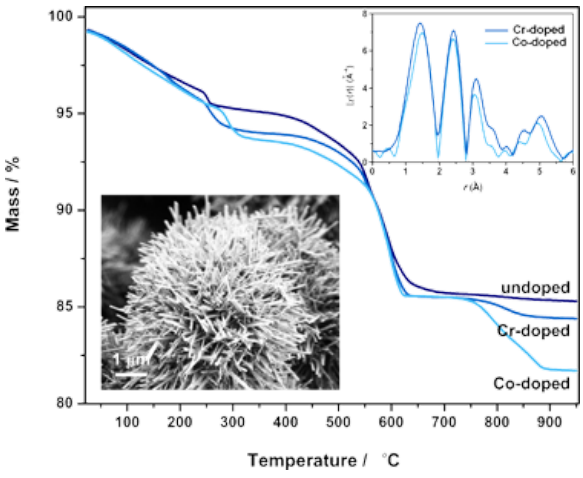

Beilstein J. Nanotechnol. **2017,** *8,* 1032–1042, doi:10.3762/bjnano.8.104

Treatment of fly ash from power plants using thermal plasma

Sulaiman Al-Mayman, Ibrahim AlShunaifi, Abdullah Albeladi, Imed Ghiloufi and Saud Binjuwair

Full Research Paper | Published 11 May 2017

PDF Album

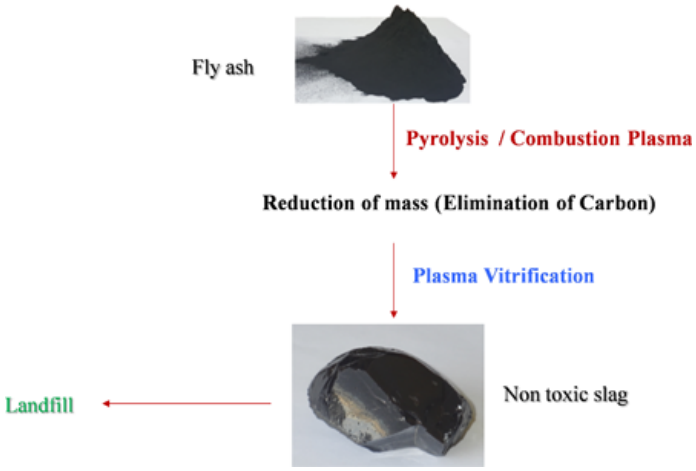

Beilstein J. Nanotechnol. **2017,** *8,* 1043–1048, doi:10.3762/bjnano.8.105

Assembly of metallic nanoparticle arrays on glass via nanoimprinting and thin-film dewetting

Sun-Kyu Lee, Sori Hwang, Yoon-Kee Kim and Yong-Jun Oh

Letter | Published 12 May 2017

PDF Album

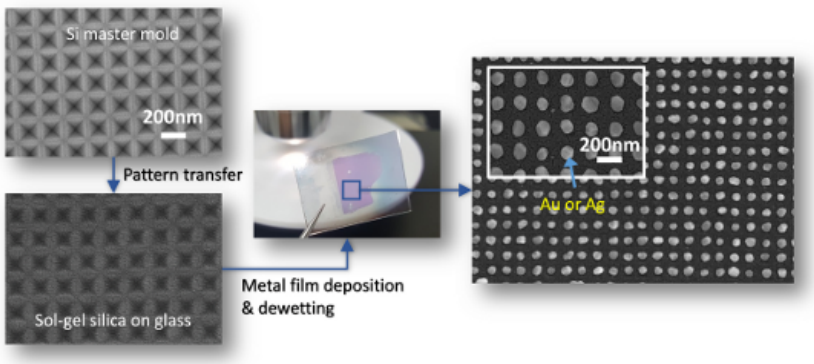

Beilstein J. Nanotechnol. **2017,** *8,* 1049–1055, doi:10.3762/bjnano.8.106

The integration of graphene into microelectronic devices

Guenther Ruhl, Sebastian Wittmann, Matthias Koenig and Daniel Neumaier

Review | Published 15 May 2017

PDF Album

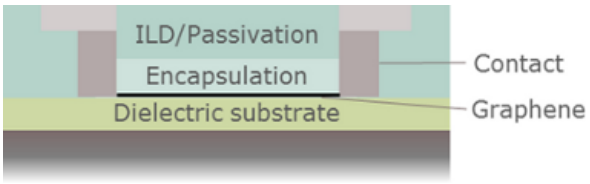

Beilstein J. Nanotechnol. **2017,** *8,* 1056–1064, doi:10.3762/bjnano.8.107

Optical response of heterogeneous polymer layers containing silver nanostructures

Miriam Carlberg, Florent Pourcin, Olivier Margeat, Judikaël Le Rouzo, Gérard Berginc, Rose-Marie Sauvage, Jörg Ackermann and Ludovic Escoubas

Full Research Paper | Published 16 May 2017

PDF Album

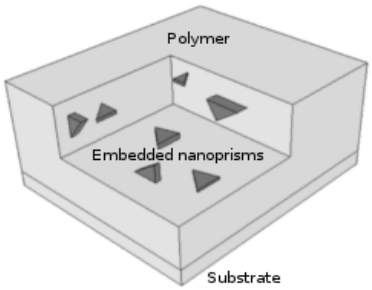

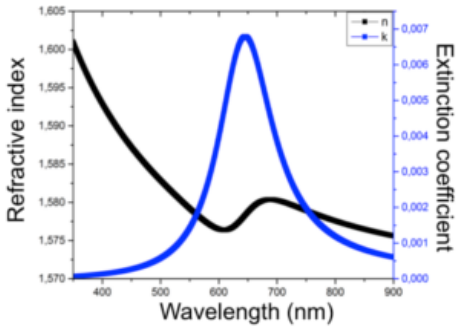

Beilstein J. Nanotechnol. **2017,** *8,* 1065–1072, doi:10.3762/bjnano.8.108

Stable Au–C bonds to the substrate for fullerene-based nanostructures

Taras Chutora, Jesús Redondo, Bruno de la Torre, Martin Švec, Pavel Jelínek and Héctor Vázquez

Full Research Paper | Published 17 May 2017

PDF Album

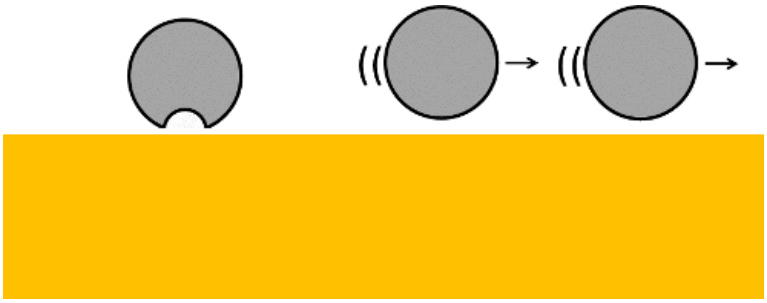

Beilstein J. Nanotechnol. **2017,** *8,* 1073–1079, doi:10.3762/bjnano.8.109

ZnO nanoparticles sensitized by $CuInZn_xS_{2+x}$ quantum dots as highly efficient solar light driven photocatalysts

Florian Donat, Serge Corbel, Halima Alem, Steve Pontvianne, Lavinia Balan, Ghouti Medjahdi and Raphaël Schneider

Full Research Paper | Published 17 May 2017

PDF Album Supp. Info

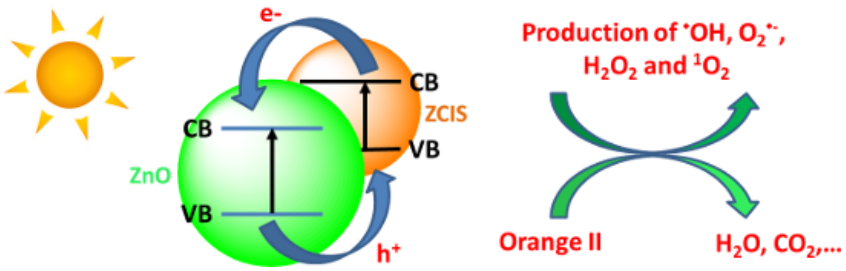

Beilstein J. Nanotechnol. **2017,** *8,* 1080–1093, doi:10.3762/bjnano.8.110

Fully scalable one-pot method for the production of phosphonic graphene derivatives

Kamila Żelechowska, Marta Prześniak-Welenc, Marcin Łapiński, Izabela Kondratowicz and Tadeusz Miruszewski

Full Research Paper | Published 18 May 2017

PDF Album Supp. Info

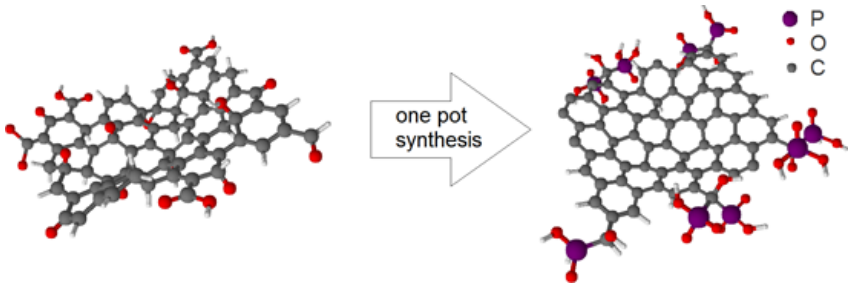

Beilstein J. Nanotechnol. **2017,** *8,* 1094–1103, doi:10.3762/bjnano.8.111

Ultrasmall magnetic field-effect and sign reversal in transistors based on donor/acceptor systems

Thomas Reichert and Tobat P. I. Saragi

Full Research Paper **Published 19 May 2017**

PDF Album Supp. Info

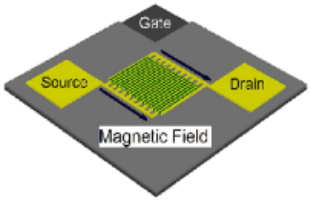

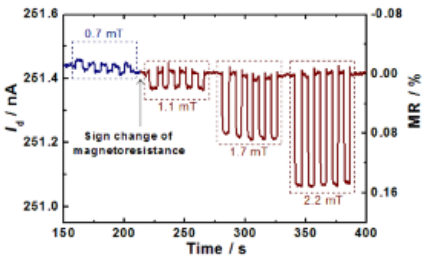

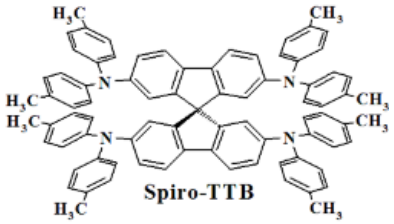

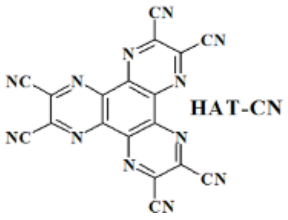

Beilstein J. Nanotechnol. **2017,** *8,* 1104–1114, doi:10.3762/bjnano.8.112

Growth, structure and stability of sputter-deposited MoS_2 thin films

Reinhard Kaindl, Bernhard C. Bayer, Roland Resel, Thomas Müller, Viera Skakalova, Gerlinde Habler, Rainer Abart, Alexey S. Cherevan, Dominik Eder, Maxime Blatter, Fabian Fischer, Jannik C. Meyer, Dmitry K. Polyushkin and Wolfgang Waldhauser

Full Research Paper **Published 22 May 2017**

PDF Album

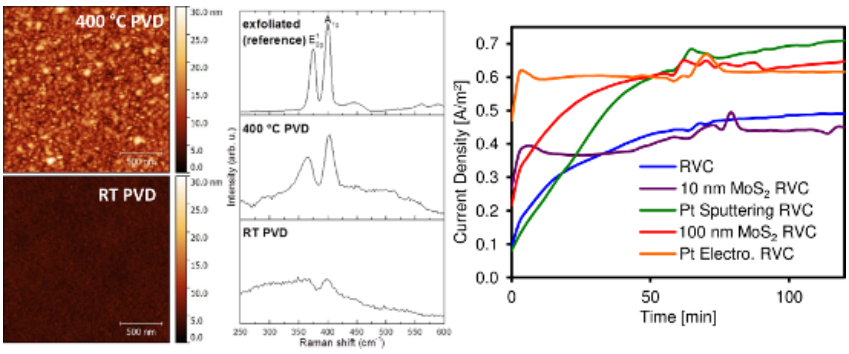

Beilstein J. Nanotechnol. **2017,** *8,* 1115–1126, doi:10.3762/bjnano.8.113

Adsorption characteristics of $Er_3N@C_{80}$ on W(110) and Au(111) studied via scanning tunneling microscopy and spectroscopy

Sebastian Schimmel, Zhixiang Sun, Danny Baumann, Denis Krylov, Nataliya Samoylova, Alexey Popov, Bernd Büchner and Christian Hess

Full Research Paper | Published 23 May 2017

PDF Album

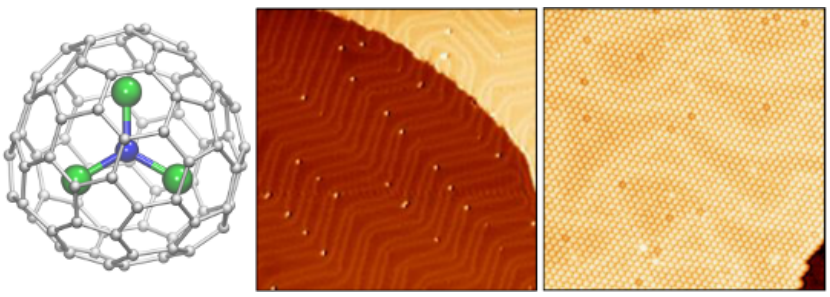

Beilstein J. Nanotechnol. **2017,** *8,* 1127–1134, doi:10.3762/bjnano.8.114

Hierarchically structured nanoporous carbon tubes for high pressure carbon dioxide adsorption

Julia Patzsch, Deepu J. Babu and Jörg J. Schneider

Full Research Paper | Published 24 May 2017

PDF Album

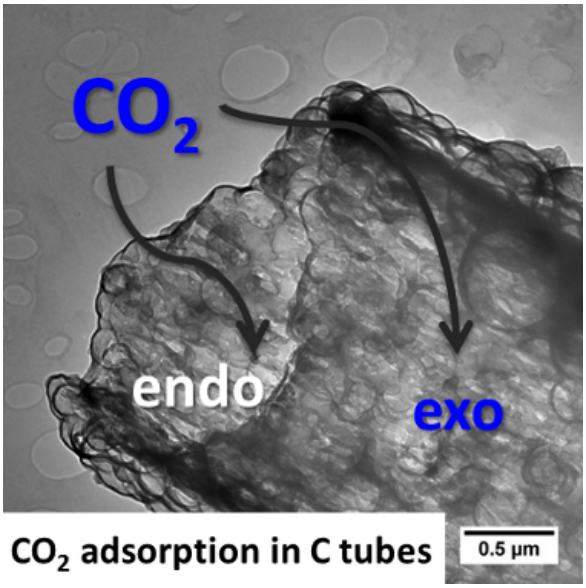

Beilstein J. Nanotechnol. **2017,** *8,* 1135–1144, doi:10.3762/bjnano.8.115

Preparation of thick silica coatings on carbon fibers with fine-structured silica nanotubes induced by a self-assembly process

Benjamin Baumgärtner, Hendrik Möller, Thomas Neumann and Dirk Volkmer

Full Research Paper | Published 26 May 2017

PDF Album Supp. Info

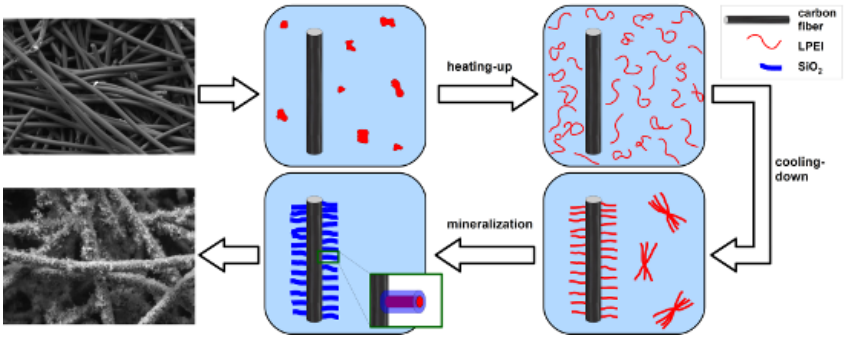

Beilstein J. Nanotechnol. **2017,** *8,* 1145–1155, doi:10.3762/bjnano.8.116

AgCl-doped CdSe quantum dots with near-IR photoluminescence

Pavel A. Kotin, Sergey S. Bubenov, Natalia E. Mordvinova and Sergey G. Dorofeev

Full Research Paper | Published 29 May 2017

PDF Album Supp. Info

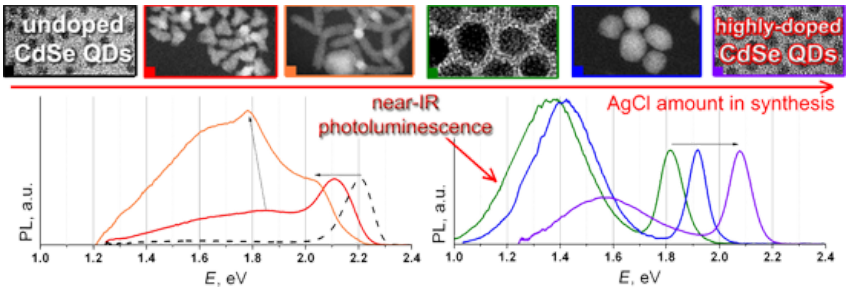

Beilstein J. Nanotechnol. **2017,** *8,* 1156–1166, doi:10.3762/bjnano.8.117

Enhanced catalytic activity without the use of an external light source using microwave-synthesized CuO nanopetals

Govinda Lakhotiya, Sonal Bajaj, Arpan Kumar Nayak, Debabrata Pradhan, Pradip Tekade and Abhimanyu Rana

Full Research Paper | Published 30 May 2017

PDF Album Supp. Info

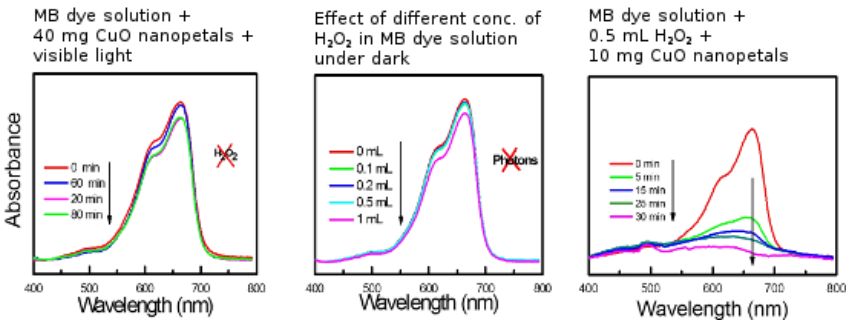

Beilstein J. Nanotechnol. **2017,** *8,* 1167–1173, doi:10.3762/bjnano.8.118

Atomic structure of Mg-based metallic glass investigated with neutron diffraction, reverse Monte Carlo modeling and electron microscopy

Rafał Babilas, Dariusz Łukowiec and Laszlo Temleitner

The 2016 Journal Impact Factor is 3.1

published on 29 Jun 2017

The 2016 Journal Impact Factor is 3.1 and the journal remained a Q1 applied physics and materials science journal.

According to the 2016 Journal Citation Reports (Clarivate Analytics, 2017), the 2016 Journal Impact Factor is 3.1 and the journal remained a Q1 applied physics and materials science journal. Additional journal bibliometrics will be published soon.

BEILSTEIN JOURNAL OF NANOTECHNOLOGY

High photocatalytic activity of Fe_2O_3/TiO_2 nanocomposites prepared by photodeposition for degradation of 2,4-dichlorophenoxyacetic acid

Shu Chin Lee[1], Hendrik O. Lintang[1,2] and Leny Yuliati[*1,2]

Full Research Paper

Open Access

Address:
[1]Centre for Sustainable Nanomaterials, Ibnu Sina Institute for Scientific and Industrial Research, Universiti Teknologi Malaysia, 81310 UTM Johor Bahru, Johor, Malaysia and [2]Ma Chung Research Center for Photosynthetic Pigments, Universitas Ma Chung, Villa Puncak Tidar N-01, Malang 65151, East Java, Indonesia

Email:
Leny Yuliati[*] - leny.yuliati@machung.ac.id

* Corresponding author

Keywords:
2,4-dichlorophenoxyacetic acid; Fe_2O_3/TiO_2; herbicide degradation; heterojunction; holes and superoxide radicals; photocatalyst; photodeposition; water purification

Beilstein J. Nanotechnol. **2017,** *8,* 915–926.
doi:10.3762/bjnano.8.93

Received: 22 December 2016
Accepted: 28 March 2017
Published: 24 April 2017

Associate Editor: R. Xu

Abstract

Two series of Fe_2O_3/TiO_2 samples were prepared via impregnation and photodeposition methods. The effect of preparation method on the properties and performance of Fe_2O_3/TiO_2 for photocatalytic degradation of 2,4-dichlorophenoxyacetic acid (2,4-D) under UV light irradiation was examined. The Fe_2O_3/TiO_2 nanocomposites prepared by impregnation showed lower activity than the unmodified TiO_2, mainly due to lower specific surface area caused by heat treatment. On the other hand, the Fe_2O_3/TiO_2 nanocomposites prepared by photodeposition showed higher photocatalytic activity than the unmodified TiO_2. Three times higher photocatalytic activity was obtained on the best photocatalyst, $Fe_2O_3(0.5)/TiO_2$. The improved activity of TiO_2 after photodeposition of Fe_2O_3 was contributed to the formation of a heterojunction between the Fe_2O_3 and TiO_2 nanoparticles that improved charge transfer and suppressed electron–hole recombination. A further investigation on the role of the active species on Fe_2O_3/TiO_2 confirmed that the crucial active species were both holes and superoxide radicals. The $Fe_2O_3(0.5)/TiO_2$ sample also showed good stability and reusability, suggesting its potential for water purification applications.

Introduction

Photocatalytic reactions have been widely suggested for environmental remediation under mild conditions. In the presence of only a photocatalyst and a light source of appropriate energy, the process can mineralize organic pollutants to harmless products such as carbon dioxide and water. Among the semiconductor photocatalysts, titanium dioxide (TiO_2) has been the foremost established material for degradation of organic pollutants [1,2]. In addition to its nontoxicity, abundance and relatively low cost, TiO_2 also shows excellent photocatalytic activity in many degradation reactions. Unfortunately, the photocatalytic

performance of TiO_2 is generally restricted by its high charge carrier recombination rate. Therefore, the modification of TiO_2 in order to reduce such recombinations remains a critical task. Another important point is the emphasis on using an environmentally safe and sustainable material as the modifier.

As one of the best modifiers, the use of a co-catalyst has been recognized to improve the photocatalytic performance of semiconductor photocatalysts as it promotes charge separation and suppresses photocorrosion of the semiconductor photocatalyst [3,4]. One of the potential co-catalyst modifiers is iron(III) oxide (Fe_2O_3), which is nontoxic, stable, cost effective and found abundantly in the earth. It has been reported that Fe_2O_3 can be used to increase the photocatalytic activity or selectivity of semiconductor photocatalysts for degradation of organic pollutants [5-15]. Commonly, the reported methods for the preparation of Fe_2O_3/TiO_2 include impregnation [5,6,16-18], sol–gel [7,19], and hydrothermal methods [8-10]. A combination of several processes has also been employed, such as the electrospinning method combined with a hydrothermal approach [11], plasma enhanced-chemical vapor deposition (PECVD) and radio frequency (RF) sputtering approach [12], and plasma enhanced-chemical vapor deposition and atomic layer deposition (ALD) followed by thermal treatment [13]. Among these preparation methods, impregnation is a commonly used approach for the preparation of Fe_2O_3/TiO_2 as it offers a simple process. However, there are contradicting reports on the performance of Fe_2O_3/TiO_2 catalysts prepared by the impregnation method. While some groups reported good photocatalytic activity [5,6], others showed contrasting results [16-18], which have resulted in different opinions regarding the contribution of the Fe_2O_3. Since the impregnation method usually involves heat treatment, the properties of TiO_2 such as the ratio of anatase/rutile, particle size, as well as specific surface area may be altered during this process and could influence the photocatalytic activity of TiO_2 [16,17]. Therefore, careful considerations shall be taken before concluding whether the Fe_2O_3 is beneficial or not in regards to improving the photocatalytic activity of TiO_2.

Another simple method to produce Fe_2O_3/TiO_2 is a mechanochemical milling approach that can be carried out at ambient conditions [14]. Even though high activity was obtained, evidence of the formation of good contact between Fe_2O_3 and TiO_2 nanoparticles was not provided. Recently, the photodeposition method has been proposed as a suitable method to directly investigate the role of added copper or lanthanum species without such heat-treatment effects [20,21]. Moreover, the modification of TiO_2 nanoparticles by photodeposition resulted in an improved photocatalytic activity as compared to unmodified TiO_2 [20-22]. Therefore, it is meaningful to employ the photodeposition method to prepare Fe_2O_3/TiO_2 catalysts without heat treatment at ambient conditions. Using iron(III) nitrate nonahydrate as the precursor, active and stable Fe_2O_3/TiO_2 was successfully prepared via photodeposition [15]. However, the actual amount of iron precursor in the prepared Fe_2O_3/TiO_2 was much lower than that added. In the present study, Fe_2O_3/TiO_2 nanocomposites were prepared by a similar approach but using iron(III) acetylacetonate as the precursor to facilitate a complete photodeposition process. The properties and activity results were compared with those prepared by the commonly used impregnation approach. Furthermore, to the best of our knowledge, there is no study on the activity comparison between Fe_2O_3/TiO_2 prepared by the widely used impregnation and the photodeposition methods, which is important to determine the optimal method for the preparation of photocatalyst materials with good properties.

In this study, both impregnation and photodeposition methods were used to modify TiO_2 nanoparticles with Fe_2O_3 in order to investigate the effect of preparation method on the properties and photocatalytic activity of the nanocomposites with respect to the degradation of 2,4-dichlorophenoxyacetic acid (2,4-D) under irradiation of UV light. 2,4-D is a herbicide widely utilized in the agricultural industry; it can be found in water sources due to its common use in controlling broadleaf weeds [23]. Excessive exposure of 2,4-D leads to adverse impacts on the ecosystem, and thus, the toxic organic pollutant must be eliminated from the water source utilizing efficient approaches. Various removal methods of 2,4-D have been developed, including adsorption [24], biodegradation [25], ozonation [26], and photocatalytic degradation [15,20-22,27-32], of which the latter has been recognized for its capability to decompose the organic pollutant under a mild environment. In the present work, it was shown that the different preparation methods resulted in distinctly different properties and photocatalytic activity. Better properties and the improved activity of Fe_2O_3/TiO_2 nanocomposites prepared by photodeposition for the degradation of 2,4-D were discussed. In addition to identifying the charge transfer capability of the Fe_2O_3/TiO_2 catalyst for improved photocatalytic activity, the role of the active species on the Fe_2O_3/TiO_2 nanocomposites prepared by the photodeposition method was further investigated in order to understand the important active species contributing to the photocatalytic activity.

Results and Discussion

Photocatalytic activity comparison

The photocatalytic efficiency of the Fe_2O_3/TiO_2 nanocomposites prepared by impregnation was evaluated for the removal of 2,4-D under UV light illumination at room temperature for 1 h. Under the same conditions, it was confirmed that no photolysis

of 2,4-D was obtained without photocatalyst. After adsorption–desorption equilibrium was achieved in 1 h, adsorption experiments were conducted in the absence of light for another 1 h. Related to the following sample descriptions, NT represents no treatment, IM indicates the samples were prepared by impregnation, PD indicates samples were prepared by photodeposition, and T indicates an additional heat treatment was carried out. Figure 1A demonstrates that the TiO_2 (NT) sample gave 30% adsorption of 2,4-D. After heat treatment at 500 °C, the adsorption of 2,4-D on the samples was greatly suppressed. All the TiO_2 (IM_T) and Fe_2O_3/TiO_2 (IM) nanocomposites showed 2,4-D adsorption of 2–3%. The photocatalytic activity of the photocatalysts was each determined by exclusion of 2,4-D adsorption and the results are shown in Figure 1B. There was no significant difference observed between the TiO_2 (NT) and the TiO_2 (IM_T), which showed 2,4-D removal of 78 and 76%, respectively. Introducing various amounts of Fe_2O_3 on the TiO_2 material via impregnation did not improve the photocatalytic activity of the TiO_2. With increased loading of Fe_2O_3, the photocatalytic performance of TiO_2 in fact decreased. As another control experiment, α-Fe_2O_3 synthesized at 500 °C for 4 h was also tested for the removal of 2,4-D. The removal of 2,4-D using α-Fe_2O_3 was only 2% after 1 h of UV illumination, which might be due to the fast charge recombination in hematite [13,15,33].

In contrast to the samples synthesized by the impregnation method, the high adsorption of 2,4-D at 25–30% was still achieved on the photodeposition synthesized samples as shown in Figure 2A. Only a slight decrease in adsorption was obtained with increasing Fe/Ti ratio, suggesting that the adsorption sites were not covered by the deposition of Fe_2O_3. Figure 2B shows the photocatalytic performance of the TiO_2 and the Fe_2O_3/TiO_2 (PD) nanocomposites after the exclusion of the 2,4-D adsorption. No significant difference in the activity was obtained for the TiO_2 (NT) and the TiO_2 (PD_T), which showed 2,4-D removal of 78 and 76%, respectively. This result clearly demonstrated that, in contrast to the heat treatment, the photodeposition treatment did not alter the photocatalytic performance of TiO_2. It is worth noting that after the Fe species were photodeposited on the TiO_2, all the nanocomposites gave superior activity as compared to that of unmodified TiO_2. The Fe/Ti ratio of 0.5 mol % was found to be the optimum loading in which the

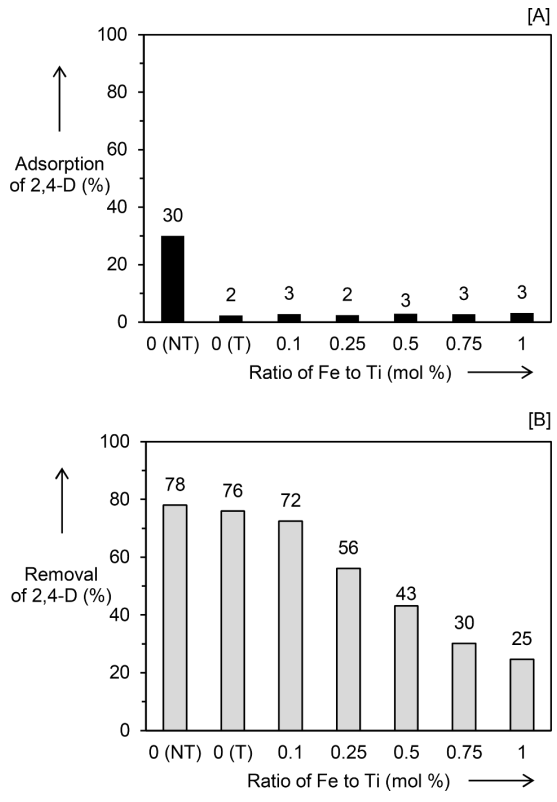

Figure 1: (A) Adsorption and (B) photocatalytic removal of 2,4-D using TiO_2 (NT), TiO_2 (IM_T) and series of Fe_2O_3/TiO_2(IM). NT represents no treatment, IM shows the samples were prepared by impregnation method, and T indicates an additional heat treatment was carried out on the sample.

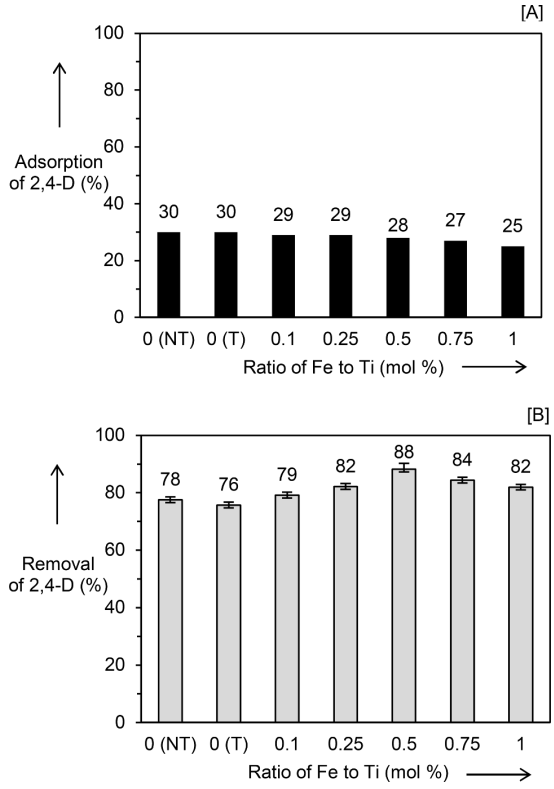

Figure 2: (A) Adsorption and (B) photocatalytic removal of 2,4-D over TiO_2 (NT), TiO_2 (PD_T) and a series of Fe_2O_3/TiO_2(PD) samples. Error bars in (B) are shown for comparison purposes. NT represents no treatment, PD shows the samples were prepared by photodeposition method, and T indicates an additional photodeposition treatment was carried out on the sample.

Fe_2O_3(0.5)/TiO_2 (PD) sample showed the highest removal of 88% after 1 h irradiation. These results showed that different synthesis methods lead to different photocatalytic performance. The photocatalysts prepared by photodeposition showed superior performance compared to those prepared by the impregnation method.

Properties comparison

The structural, optical, and physical properties of the Fe_2O_3/TiO_2 photocatalysts synthesized by impregnation and photodeposition were investigated and compared to clarify the characteristic differences of the photocatalysts obtained from the different preparation methods. X-ray diffraction (XRD) patterns were collected for the Fe_2O_3/TiO_2 (IM) series prepared by the impregnation method. TiO_2 (NT) exhibited diffraction peaks corresponding to the anatase phase (JCPDS file No. 21-1272), which were observed at 2θ of 25.35, 38.10, 48.05, 54.55, and 62.60°, corresponding to (101), (004), (200), (105), and (204) diffraction planes, respectively (see Supporting Information File 1, Figure S1). After heat treatment, the TiO_2 (IM_T) sample showed improved crystallinity without any changes in the structural phase, which was found to be pure anatase. After addition of Fe species, the crystallinity of the Fe_2O_3/TiO_2 (IM) nanocomposites did not change and was confirmed to be similar to that of the TiO_2 (IM_T) sample. The characteristic diffraction peaks corresponding to the anatase phase of TiO_2 remained in all samples without any peak shifting. Furthermore, the existence of new diffraction peaks of α-Fe_2O_3 (JCPDS file No. 33-0664) was not identified, suggesting that the low loading of Fe_2O_3 might be dispersed well on the surface of the TiO_2.

The Scherrer equation was used to calculate the crystallite size of the samples based on the (101) peak at 2θ of 25.35°. As listed in Table 1, the crystallite size of the TiO_2 (NT) was initially 9.3 nm (Table 1, entry 1). After heat treatment, the crystallite size of TiO_2 (IM_T) increased to 14.3 nm (Table 1, entry 2). The addition of Fe_2O_3 did not further influence the crystallite size. All the Fe_2O_3/TiO_2 (IM) nanocomposites had a crystallite size in a range of 14.3–15.9 nm (Table 1, entries 3–7), which was close to that of the TiO_2 (IM_T). Since there was no much difference in the crystallinity and crystallite size between the TiO_2 (IM_T) and Fe_2O_3/TiO_2 (IM), it was suggested that the improved crystallinity and crystallite size as compared to TiO_2 (NT) was mostly due to the heat treatment only and not to the addition of Fe_2O_3.

The XRD patterns of the Fe_2O_3/TiO_2 (PD) series that was synthesized by the photodeposition method were also recorded (see Supporting Information File 1, Figure S2). Different from the case of heat treatment with the impregnation method, the photodeposition treatment did not change the crystallinity of both the TiO_2 (PD_T) and the Fe_2O_3/TiO_2 (PD) nanocomposites. No peak shifting and the appearance of no new diffraction peak suggested good dispersion of the Fe species on the surface of the TiO_2. The crystallite size of the Fe_2O_3/TiO_2 (PD) is given in Table 1. All samples have a crystallite size in the range of 8.8–9.3 nm (Table 1, entries 8–13), suggesting that the crystallite size was not altered by the photodeposition method. Comparing the two synthesis methods, it was obvious that the photodeposition method maintained both crystallinity and crystallite size of the TiO_2, while the impregnation method led to higher crystallinity and crystallite size. This difference was caused by the different preparation conditions; the photodeposition was conducted under mild synthesis conditions under illumination of UV light at room temperature, whereas a high heating temperature of 500 °C was used during the impregnation method.

Table 1: Crystallite size and band gap energy (E_g) of the unmodified TiO_2 and Fe_2O_3/TiO_2nanocomposites prepared by impregnation (IM) and photodeposition (PD) methods. NT represents no treatment and T indicates an additional heat treatment was carried out on the sample.

Entry	Samples	Crystallite size (nm)[a]	E_g (eV)[b]
1	TiO_2 (NT)	9.3	3.30
2	TiO_2 (IM_T)	14.3	3.29
3	Fe_2O_3(0.1)/TiO_2 (IM)	14.3	3.29
4	Fe_2O_3(0.25)/TiO_2 (IM)	15.9	3.27
5	Fe_2O_3(0.5)/TiO_2 (IM)	15.8	3.27
6	Fe_2O_3(0.75)/TiO_2 (IM)	15.8	3.26
7	Fe_2O_3(1)/TiO_2 (IM)	15.8	3.25
8	TiO_2 (PD_T)	8.8	3.29
9	Fe_2O_3(0.1)/TiO_2 (PD)	9.3	3.28
10	Fe_2O_3(0.25)/TiO_2 (PD)	8.8	3.27
11	Fe_2O_3(0.5)/TiO_2 (PD)	8.8	3.27
12	Fe_2O_3(0.75)/TiO_2 (PD)	8.8	3.25
13	Fe_2O_3(1)/TiO_2 (PD)	9.3	3.24

[a]Scherrer equation was used to calculate the crystallite size.
[b]Tauc plot was used to determine the E_g.

The optical absorption properties of the nanocomposites prepared by the impregnation method were investigated (see Supporting Information File 1, Figure S3). The TiO_2 (NT) sample absorbs light in the UV region and exhibits a characteristic band for TiO_2 at about 370 nm due to the charge transfer of $O^{2-} \rightarrow Ti^{4+}$ and electron excitation from the valence band (VB) to the conduction band (CB) [7,20,21]. Both the heat treatment and addition of Fe species did not affect the light absorption of the TiO_2 (NT) in the UV and visible region. Owing to the low loading of Fe, there was no additional absorption peak corre-

sponding to the Fe species. The bandgap energy (E_g) of the unmodified TiO_2 and the nanocomposites were studied by a Tauc plot, considering the indirect transition in anatase TiO_2 [34]. The Tauc plot of the TiO_2 (NT) and the Fe_2O_3/TiO_2 (IM) nanocomposites was derived by plotting $(\alpha h\nu)^{1/2}$ versus $h\nu$. The E_g value was obtained from the x-intercept using the linear extrapolation in the plot. Table 1 summarizes the E_g values of the samples. The TiO_2 (NT) sample has an E_g of 3.30 eV (Table 1, entry 1). The heat-treated TiO_2 (IM_T) showed an E_g value of 2.29 eV (Table 1, entry 2), close to the value of the TiO_2 (NT), indicating that a high calcination temperature of 500 °C did not affect the optical properties of the TiO_2. The addition of Fe species did not result in significant changes to the E_g of the TiO_2, which with an increasing Fe/Ti ratio from 0.1 to 1 mol % only slightly reduced the E_g from 3.29 to 3.25 eV (Table 1, entries 3–7). The insignificant change in the E_g suggested that the Fe species might be loaded on the surface instead of incorporated into the TiO_2 lattice. The obtained results matched well with the nanocomposite prepared via adsorption and decomposition of the Fe(III) complex at 400 °C [5]. This is in contrast to the one prepared by the sol–gel method that showed an obviously reduced E_g value as the Fe ions were incorporated into the TiO_2 lattice [7,19].

Diffuse reflectance (DR) UV–vis spectra and Tauc plots of the nanocomposites prepared by the photodeposition method were also measured (see Supporting Information File 1, Figure S4). Similar to the nanocomposites prepared by the impregnation method, the photodeposition treatment and addition of Fe species also did not much affect the light absorption or the E_g of both the TiO_2 (PD_T) and Fe_2O_3/TiO_2 (PD) sample. Besides, the slightly decreased E_g from 3.28 to 3.24 eV (Table 1, entries 9–13) also suggested that Fe species might be loaded on the surface of the TiO_2 via photodeposition.

The amount of Fe content loaded on the Fe_2O_3/TiO_2 nanocomposites was determined by the inductively coupled plasma optical emission spectrometer (ICP-OES) measurement, as listed in Table 2. The Fe/Ti composition (mol %) obtained from the measurement confirmed that the Fe content loaded on the TiO_2 was close to the nominal added amount. These results clearly suggested that in the given range of Fe loading (0.1–1 mol %), all the iron precursor was successfully photodeposited onto the TiO_2.

The Brunauer–Emmett–Teller (BET) specific surface area of the TiO_2 and the Fe_2O_3/TiO_2 nanocomposites prepared by the impregnation and the photodeposition methods are shown in Figure 3. The TiO_2 (NT) has a large specific surface area of 298 m^2/g. After calcination at 500 °C, the specific surface area of the TiO_2 (IM_T) dropped drastically to 80 m^2/g. The addition of Fe_2O_3 to TiO_2 via the impregnation method did not significantly change the specific surface area of the TiO_2 (IM_T), given that all nanocomposites have values in the range of 72–80 m^2/g. This result obviously showed that it was the heat treatment and not the Fe_2O_3 addition that caused the decrease in the BET specific surface area.

Table 2: The composition of the Fe_2O_3/TiO_2 (PD) nanocomposites (ratio of Fe/Ti (mol %)) determined from ICP-OES measurements. PD indicates samples that were prepared with the photodeposition method.

Samples	Fe/Ti (mol %)
$Fe_2O_3(0.1)/TiO_2$ (PD)	0.11
$Fe_2O_3(0.25)/TiO_2$ (PD)	0.20
$Fe_2O_3(0.5)/TiO_2$ (PD)	0.45
$Fe_2O_3(0.75)/TiO_2$ (PD)	0.72
$Fe_2O_3(1)/TiO_2$ (PD)	1.02

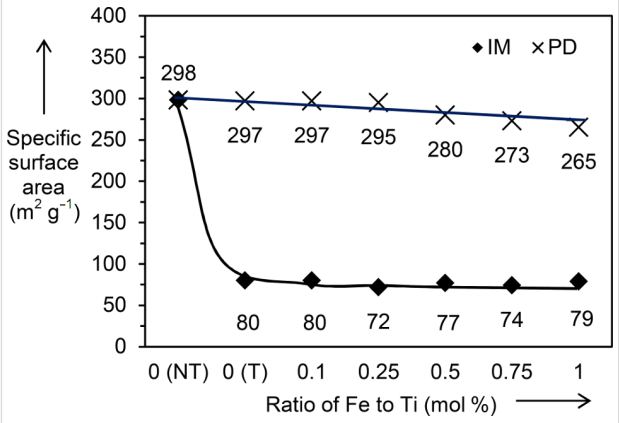

Figure 3: BET specific surface area of TiO_2 (NT), TiO_2 (T) and the series of Fe_2O_3/TiO_2 samples prepared by both impregnation (IM) and photodeposition (PD). NT represents no treatment and T indicates an additional heat treatment or photodeposition treatment was carried out on the sample.

In contrast to the nanocomposites prepared by the impregnation method, only a slight gradual decrease was observed with increasing Fe/Ti ratio in the Fe_2O_3/TiO_2 nanocomposites prepared from the photodeposition method. The nanocomposite sample with the lowest Fe/Ti ratio of 0.1 mol % still showed a large surface area of 297 m^2/g, while the nanocomposite sample with the highest Fe/Ti ratio of 1 mol % showed a value of 265 m^2/g. These results again confirmed that the mild photodeposition method did not influence the properties of the TiO_2 (NT).

As shown in Figure 1 and Figure 2, nanocomposites synthesized by the photodeposition method exhibited superior adsorp-

tion and photocatalytic activity than those synthesized by the impregnation method. The higher percentage of 2,4-D adsorption could result from the larger BET specific surface area of the samples prepared by the photodeposition method. As for the photocatalytic activity, a few important parameters have been reported to contribute to a high photocatalytic activity, including high crystallinity [35], small crystallite size [36], and high specific surface area [30,36]. Generally, materials with high crystallinity have fewer crystal defects, while a smaller crystallite size decreases the diffusion path length between the charge carriers − these two parameters can suppress recombination of photogenerated electrons−holes. On the other hand, materials with a large specific surface area have many available surface active sites for reaction to take place, which can lead to high photocatalytic activity. In the case of nanocomposites prepared by the impregnation method, even though improved crystallinity was observed, it might be compensated by the larger crystallite size and a lower specific surface area, which overall led to decreased photocatalytic activity. Since the photodeposition method did not have a great influence on the crystallinity, crystallite size, and the BET specific surface area, the effects caused by such changes can be avoided, and the main factors contributing to the photocatalytic activity can be narrowed down solely to the added Fe species.

Improved properties

Since nanocomposites synthesized by the photodeposition method showed better photocatalytic activity than the nanocomposites synthesized by the impregnation method, further detailed investigations were carried out on nanocomposites synthesized by the photodeposition method. Transmission electron microscopy (TEM) and high-resolution TEM (HRTEM) images of both unmodified TiO_2 (NT) and Fe_2O_3(0.5)/TiO_2 (PD) are shown in Figure 4. As shown in Figure 4a, the TiO_2 (NT) sample has spherical particles with a diameter of 7–9 nm. This result agreed well with the crystallite size calculated by the Scherrer equation previously discussed. The HRTEM image of the TiO_2 (NT) sample displayed in Figure 4b shows a lattice fringe spacing of 0.35 nm attributed to the anatase TiO_2(101) crystal plane. Figure 4d shows a HRTEM image of Fe_2O_3(0.5)/TiO_2 (PD). It was evident that the deposition of Fe did not change the morphology of the TiO_2. Since the lattice fringe spacing of 0.27 nm related to the Fe_2O_3(104) crystal plane was observed, the possible formation of a heterojunction between Fe_2O_3 and TiO_2 was considered. Such close contact would cause the carrier diffusion length to be short, and in turn, would improve the charge transfer. This would thus suppress charge recombination, which is crucial to enhance the photocatalytic activity.

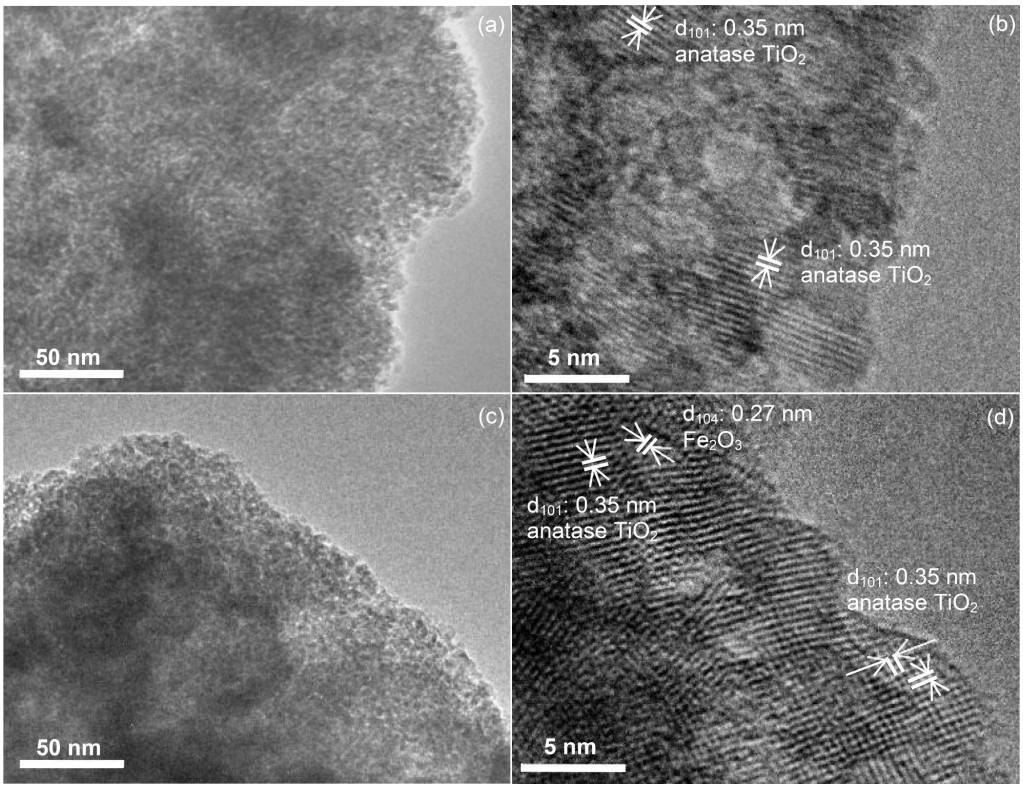

Figure 4: (a) TEM image of unmodified TiO_2 (NT) and (b) its respective HRTEM image, (c) TEM image of Fe_2O_3(0.5)/TiO_2 (PD) and (d) its respective HRTEM image.

The formation of Fe_2O_3 was in good agreement with other reported photodeposition methods when using a different iron precursor, Fe(III) nitrate nonahydrate [15]. Due to the oxidative condition during the synthesis process, the Fe(III) acetylacetonate precursor could be decomposed to Fe_2O_3 such as by the photogenerated oxygen radicals [21]. It was demonstrated that the use of the Fe(III) acetylacetonate precursor led to a complete photodeposition to form Fe_2O_3, as also supported by ICP-OES results discussed above.

The improved charge transfer of the $Fe_2O_3(0.5)/TiO_2$ (PD) sample was further clarified using electrochemical impedance spectroscopy (EIS). Figure 5 shows the Nyquist plots of the unmodified TiO_2 (NT) and $Fe_2O_3(0.5)/TiO_2$ (PD) samples. The arc radius of the Nyquist plot reflects the impedance of the interface layer arising at the electrode surface. The smaller the arc radius the better the charge transfer [37]. It is worth noting here that the $Fe_2O_3(0.5)/TiO_2$ (PD) material has a smaller arc radius than unmodified TiO_2. These results clearly suggest that the $Fe_2O_3(0.5)/TiO_2$ (PD) material has a lower impedance than unmodified TiO_2, indicating enhanced conductivity of TiO_2 after photodeposition of Fe_2O_3. The electron transfer kinetics of a material can be calculated using Equation 1:

$$k = \frac{RT}{n^2F^2AR_{ct}C^\circ} \quad (1)$$

where k is the heterogeneous electron-transfer rate constant, R is the gas constant, T is temperature (K), n represents the number of transferred electrons per molecule of the redox probe, F is the Faraday constant, A is the electrode area (cm^2), R_{ct} is the charge transfer resistance that can be obtained from the fitted Nyquist plot, and C° is the concentration of the redox couple in the bulk solution (ferricyanide/ferrocyanide) [38].

From the fitted impedance data shown in Figure 5, the $Fe_2O_3(0.5)/TiO_2$ (PD) material gave an R_{ct} value of 2.87 kΩ, which was smaller than that of unmodified TiO_2 (NT) with R_{ct} = 3.40 kΩ. The lower R_{ct} value obviously suggested that the $Fe_2O_3(0.5)/TiO_2$ (PD) material has better charge conductivity and transfer capability than unmodified TiO_2 (NT). Furthermore, the k values of the $Fe_2O_3(0.5)/TiO_2$ (PD) sample and unmodified TiO_2 (NT) were calculated to be 2.96×10^{-4} and 2.49×10^{-4} cm/s, respectively, indicating that the charge transfer that on the $Fe_2O_3(0.5)/TiO_2$ (PD) sample proceeded faster than on unmodified TiO_2. As suggested from the HRTEM result, the formation of an Fe_2O_3/TiO_2 heterojunction might promote better electron transfer which resulted in improved photocatalytic activity of the $Fe_2O_3(0.5)/TiO_2$ (PD) material.

Photoluminescence has been associated with electron–hole recombination of a photocatalyst [39]. In this study, the ability of an Fe_2O_3 co-catalyst to accept photogenerated electrons as well as to suppress the recombination of electron–holes on the TiO_2 was supported by the fluorescence spectroscopy results. The emission spectra of the unmodified TiO_2 (NT) and the $Fe_2O_3(0.5)/TiO_2$ (PD) samples under a fixed excitation wavelength of 218 nm are shown in Figure 6. TiO_2 exhibited three emission peaks at 407, 466 and 562 nm. The emission at 407 nm could be caused by the radiative recombination of self-trapped excitons, while peaks at 466 and 562 nm were attributed to the charge transfer of an oxygen vacancy trapped electron. The obtained results agreed well with the reported literature [39]. The $Fe_2O_3(0.5)/TiO_2$ (PD) material showed a decreased emission intensity as compared to the unmodified TiO_2 (NT), suggesting that the photogenerated electrons on TiO_2 could be transferred and trapped by Fe_2O_3. This resulted in a suppression of the electrons−hole recombination on TiO_2, which led to the improved removal of 2,4-D.

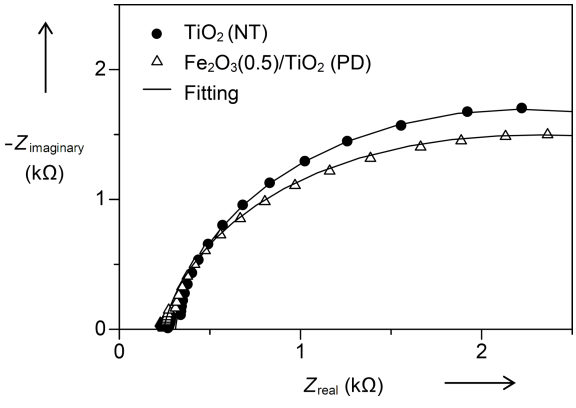

Figure 5: Nyquist plots of unmodified TiO_2 (NT) and $Fe_2O_3(0.5)/TiO_2$ (PD) with the respective model fitting.

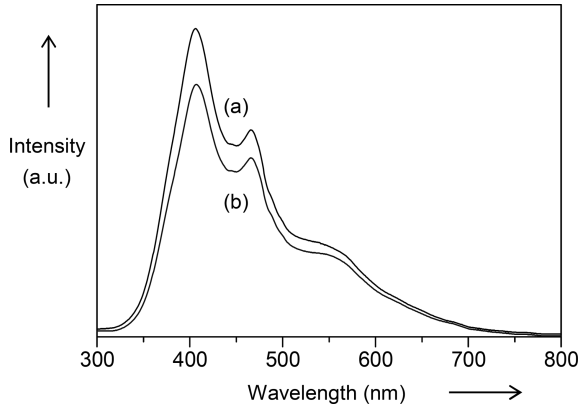

Figure 6: Emission spectra of (a) unmodified TiO_2 (NT) and (b) $Fe_2O_3(0.5)/TiO_2$ (PD).

For comparison, a Nyquist plot and emission spectrum of the $Fe_2O_3(0.1)/TiO_2$ (IM) material were also measured and given in Supporting Information File 1, Figures S5 and S6, respectively. It was clear that the $Fe_2O_3(0.1)/TiO_2$ (IM) had a smaller arc radius of the Nyquist plot and slightly lower emission intensity than the TiO_2 (NT), suggesting that the $Fe_2O_3(0.1)/TiO_2$ (IM) has better charge transfer and suppressed electron–hole recombination. Unfortunately, these better properties did not promote the photocatalytic activity of the $Fe_2O_3(0.1)/TiO_2$ (IM). It turns out that the photocatalytic activity of $Fe_2O_3(0.1)/TiO_2$ (IM) would be more influenced by the distinct decrease in the specific surface area, as discussed previously.

Active species and stability

It has been reported that the reaction pathways for photocatalytic oxidation of organic pollutants are dominated by several active species, such as holes, superoxide radicals, and hydroxyl radicals [39]. Among the scavengers of active species, ammonium oxalate has been reported as an efficient hole scavenger [40], benzoquinone acts to scavenge superoxide radicals efficiently [40], while *tert*-butanol has fast reaction with hydroxyl radicals [27,40] and hence, they were selected for the scavenger studies. As shown in Figure 7, the photocatalytic reactions under 1 h of UV illumination were evaluated in the presence of each scavenger on the unmodified TiO_2 (NT) and the $Fe_2O_3(0.5)/TiO_2$ (PD). For the reaction conducted on the unmodified TiO_2 (NT), the addition of ammonium oxalate was found to drastically suppress the activity, which was reduced from 78 to 13%, equivalent to 5.8 times lower than the one without scavenger. The inhibited activity indicated the importance of the photogenerated holes for the oxidation of 2,4-D. When benzoquinone was added, the activity was reduced from 78 to 66%, suggesting that superoxide radicals also played a role in the oxidation process of 2,4-D. In contrast, addition of *tert*-butanol did not affect the activity of the TiO_2 (NT), indicating that hydroxyl radicals are not the important active species for the reaction.

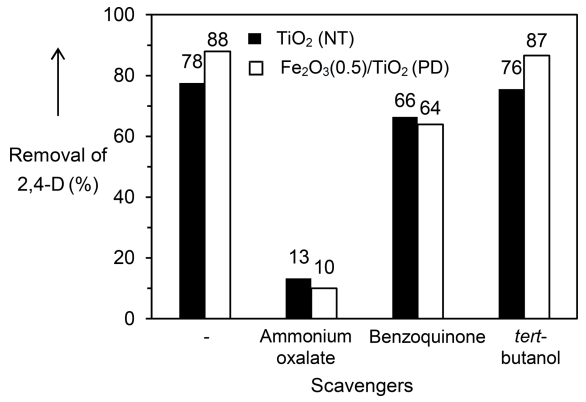

Figure 7: Percentage removal of 2,4-D on unmodified TiO_2 (NT) and $Fe_2O_3(0.5)/TiO_2$ (PD) in the absence and presence of various scavengers under UV light irradiation for 1 h.

Since the photogenerated holes on the TiO_2 have strong oxidizing power among oxidizing species [41], it is reasonable that holes are the most dominate active species in the oxidation of 2,4-D. Moreover, it has been reported that the oxidation of 2,4-D via a direct holes mechanism was favored at pH 3 [27]. In this study, an initial pH for 2,4-D was confirmed to be 3.2. On the other hand, superoxide radicals could be also easily formed for the oxidation reaction since the reaction was conducted in an open reactor, whereby the reduction of oxygen can easily take place. Related to the formation of hydroxyl radicals, it has been revealed that more hydroxyl radicals are formed from the adsorbed hydroxide ions with increased pH [28,42]. Therefore, it is likely that under the present conditions, they did not contribute as the active species probably due to their low formation.

The scavenger study was also conducted using the $Fe_2O_3(0.5)/TiO_2$ (PD) as shown in Figure 7. It was clear that the $Fe_2O_3(0.5)/TiO_2$ (PD) gave similar trend of activity as the ones obtained on the unmodified TiO_2 (NT). Both the photogenerated holes and superoxide radicals were important species, while hydroxyl radicals did not give much influence on the photocatalytic oxidation of 2,4-D. As compared to the unmodified TiO_2 (NT), the $Fe_2O_3(0.5)/TiO_2$ (PD) showed a more drastic reduction in the activity when the reactions were conducted in the presence of holes and superoxide radical scavengers. The activity decreased 8.8 and 1.4 times, respectively, as compared to those on TiO_2 (NT), i.e., 5.8 and 1.2 times, respectively. Such a result suggested the crucial role of Fe_2O_3 as a co-catalyst to improve the interfacial charge transfer and suppress electron–hole recombination. This leads to the formation of more photogenerated holes and superoxide radicals that contributed to an improved photocatalytic activity, as was also supported by the HRTEM, EIS and fluorescence spectroscopy results.

The stability of the $Fe_2O_3(0.5)/TiO_2$ (PD) sample was investigated by performing several cycles of photocatalytic reactions under UV light irradiation for 1 h. The $Fe_2O_3(0.5)/TiO_2$ (PD) sample gave a similar, comparable activity in a range of 82–88% even after 3 cycles of reactions, suggesting the good photostability of the $Fe_2O_3(0.5)/TiO_2$ (PD) nanocomposite and its potential application for photocatalytic water purification.

Degradation and proposed mechanism

After the photocatalytic reactions on all samples, the formation of a 2,4-dichlorophenol (2,4-DCP) intermediate was observed

from the HPLC analysis, which was in good agreement with reported studies [15,28-32]. The 2,4-D degradation was then determined by Equation 2:

$$\text{2,4-D degradation}(\%) = \frac{[\text{2,4-D}]_\text{I} - [\text{2,4-D}]_\text{F} - [\text{2,4-DCP}]}{[\text{2,4-D}]_\text{I}} \times 100\% \quad (2)$$

where $[2,4\text{-D}]_I$ represents the initial concentration of 2,4-D after reaching adsorption–desorption equilibrium under dark conditions, $[2,4\text{-D}]_F$ is the final concentration of 2,4-D after lamp exposure and [2,4-DCP] is the concentration of the formed 2,4-DCP intermediate after lamp exposure. The percentage of 2,4-D degradation on the unmodified TiO_2 and the Fe_2O_3/TiO_2 (PD) series is given in Figure 8. Unmodified TiO_2 (NT) and TiO_2 (PD_T) showed a comparable degradation of 2,4-D of 6 and 5%, respectively. The addition of Fe_2O_3 was demonstrated to improve the photocatalytic activity of TiO_2 for degradation of 2,4-D. The $Fe_2O_3(0.5)/TiO_2$(PD) showed a 2,4-D degradation of 18%, which was three times higher than the unmodified TiO_2 (NT). Such enhanced performance was only slightly higher than that reported when using a Fe(III) nitrate nonahydrate precursor, which gave more than two times higher activity than the bare TiO_2 [15].

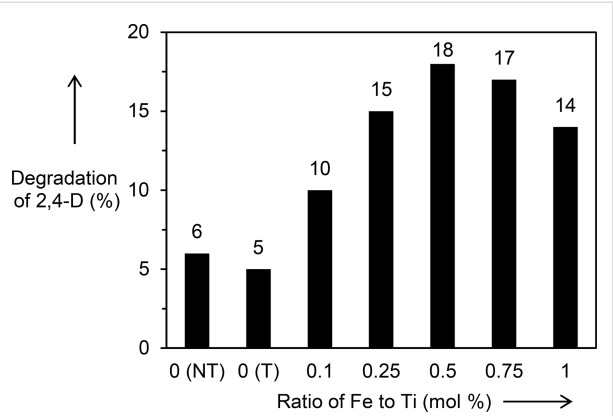

Figure 8: Photocatalytic degradation of 2,4-D on TiO_2 (NT), TiO_2 (PD_T) and the series of Fe_2O_3/TiO_2(PD) samples. NT represents no treatment, PD shows the samples were prepared by photodeposition method, and T indicates an additional photodeposition treatment was carried out on the sample.

The photocatalytic oxidation of 2,4-D by active species involves various steps, including formation of intermediates before its mineralization to CO_2 and H_2O. Decarboxylation has been reported as the initial step during the photocatalytic oxidation of 2,4-D when it is carried out at pH 3 [27]. The benzene ring opening and hydrocarbon chain breaking then took place, which finally led to the formation of CO_2 [29]. Since 2,4-DCP was detected as the dominant intermediate after the photocatalytic reactions, it could be suggested that 2,4-D was firstly oxidized by the active species (photogenerated holes and superoxide radicals) before decarboxylation and the formation of 2,4-DCP. The dechlorination of 2,4-DCP then took place, leading to ring opening, hydrocarbon chain breaking, and finally, the mineralization to CO_2 and H_2O (see Supporting Information File 1, Figure S7).

The mechanism of major charge transfer pathways on the $Fe_2O_3(0.5)/TiO_2$ (PD) was also proposed and shown in Figure 9. When the photocatalyst is exposed to UV light, photo-

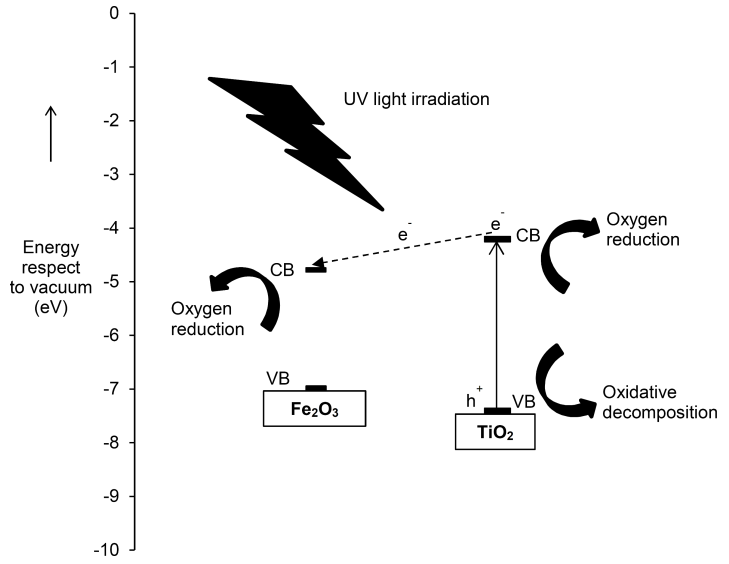

Figure 9: Proposed mechanism for major charge transfer pathways on $Fe_2O_3(0.5)/TiO_2$ (PD) for degradation of 2,4-D.

generated electrons are excited from the VB to the CB of TiO_2, while photogenerated holes are left in the VB. The photogenerated electrons could reduce oxygen to form superoxide radicals, while holes could directly oxidize 2,4-D to 2,4-DCP before its mineralization. The presence of Fe_2O_3 reduces electron–hole recombination on the TiO_2. Since the CB edge energy level of Fe_2O_3 (−4.78 eV relative to absolute vacuum scale (AVS)) is lower than that of TiO_2 (−4.21 eV relative to AVS) [43], Fe_2O_3 could act as an electron trapper that captured the photogenerated electrons from the TiO_2 that were not used for reduction of oxygen, instead of recombination with holes. Such electron transfer could suppress charge recombination on TiO_2 [5,10,12,14,15], whereby the oxidation of 2,4-D still could occur in the VB of TiO_2, and therefore, the photocatalytic degradation of 2,4-D could be improved. On the other hand, owing to the fast recombination of holes and electrons, the photocatalytic degradation of 2,4-D on bare Fe_2O_3 was negligible (1%). The oxidation of 2,4-D is unlikely to take place in the valence band of Fe_2O_3 and this would be the very minor pathway. Similar mechanisms have been also reported elsewhere [15].

Conclusion

Two series of Fe_2O_3/TiO_2 nanocomposites were prepared by the impregnation and the photodeposition methods. The Fe_2O_3/TiO_2 nanocomposites prepared by the impregnation method showed less activity than the unmodified TiO_2 (NT), which was mainly due to the lower specific surface area caused by heat treatment. On the other hand, all the Fe_2O_3/TiO_2 nanocomposites prepared by the photodeposition methods exhibited superior photocatalytic activity as compared to the unmodified samples. The good photocatalytic activity of the nanocomposites was associated with the formation of a heterojunction between Fe_2O_3 and TiO_2 nanoparticles that promoted good charge transfer and suppressed electron–hole recombination. Scavenger studies showed that the photogenerated holes and superoxide radicals were the important active species in the reaction. The $Fe_2O_3(0.5)/TiO_2$ material showed excellent stability and reusability for the removal of 2,4-D. Among the nanocomposites, the $Fe_2O_3(0.5)/TiO_2$ sample showed the best activity, exhibiting 18% degradation of 2,4-D after 1 h of reaction, corresponding to three times higher activity compared to unmodified TiO_2.

Experimental

Materials

All chemicals and materials in the experiments were used without supplementary purification. The chemicals used were commercial Hombikat UV100 TiO_2 (UV100, Sachtleben Chemie), iron(III) acetylacetonate (99.9%, Sigma–Aldrich), ethanol (99.98%, HmbG® Chemicals), sodium sulfate (99.0%, Fisher Chemical), potassium ferricyanide (99.0%, Riedel-de Haën), 2,4-D (98.0%, Sigma), ammonium oxalate (99.5–101%, Merck), benzoquinone (99%, Acros Organics), and *tert*-butanol (99.0%, Merck).

Sample preparation

The TiO_2 material used in this study was from the commercial supplier Hombikat, UV100 TiO_2. The Fe_2O_3 used as a control was prepared by direct calcination of Fe(III) acetylacetonate under air atmosphere at 500 °C for 4 h. Two series of Fe_2O_3/TiO_2 nanocomposites were prepared by impregnation and photodeposition methods. As for the synthesis of the nanocomposites via the impregnation method, an appropriate amount of Fe(III) acetylacetonate with varying mole percentage (mol %) of Fe/Ti of 0.1, 0.25, 0.5, 0.75 and 1 mol % were firstly dissolved in mixed solvents of water and ethanol (20 mL). Then, the commercial Hombikat UV100 TiO_2 (1 g) was dispersed in the Fe(III) acetylacetonate solution for 10 min by an ultrasonicator. The mixture was stirred and heated at 80 °C until all solvents were completely evaporated. The grind dried solid powder was then calcined at a temperature of 500 °C for 4 h. The prepared samples were labelled as $Fe_2O_3(x)/TiO_2$ (IM), where x relates to the loading of Fe/Ti in mol %. Bare TiO_2 with a similar heat treatment without the addition of the iron precursor was also prepared and denoted as TiO_2 (IM_T), while the TiO_2 without any pretreatment was denoted as TiO_2 (NT).

As for synthesis of the nanocomposites via the photodeposition method [20-22], an appropriate amount of Fe(III) acetylacetonate with various mole percentages of Fe/Ti (0.1, 0.25, 0.5, 0.75 and 1 mol %) were firstly dissolved in mixed solvents of water and ethanol (20 mL) by ultrasonication for few minutes. Then, the commercial Hombikat UV100 TiO_2 (1 g) was dispersed in the Fe(III) acetylacetonate solution by ultrasonic mixing for 10 min. The mixture was then stirred and irradiated under a 200 W Hg−Xe lamp (Hamamatsu, light intensity of 8 mW/cm^2 at 365 nm) at room temperature for 5 h. The solid was washed a few times with ethanol followed by deionized water before drying overnight inside an oven at 80 °C. Finally, the obtained solid powder was ground. The prepared samples were denoted as $Fe_2O_3(x)/TiO_2$ (PD), where x relates to the loading of Fe/Ti (in mol %). Bare TiO_2 undergoing a similar photodeposition treatment without the addition of the iron precursor was also produced and was denoted as TiO_2 (PD_T).

Sample characterization

A Bruker D8 Advance diffractometer was used to measure the XRD patterns of the TiO_2 and the Fe_2O_3/TiO_2 samples prepared by both impregnation and photodeposition methods using a Cu Kα radiation source (λ = 0.15406 nm) at 40 kV and 40 mA. A Shimadzu UV-2600 DR UV−vis spectrophotometer was used to record the absorption spectra of samples, in which barium sulfate ($BaSO_4$) was used as a reference. The elemental

compositions (Fe, Ti) on the Fe_2O_3/TiO_2 (PD) nanocomposites were determined using an Agilent 700 series ICP-OES. The adsorption of nitrogen gas on the samples was measured at 77 K on a Quantachrome Novatouch LX4 instrument in order to determine the BET specific surface area of the samples.

TEM and HRTEM were performed on a JEOL JEM-2100 electron microscope with electron acceleration energy of 200 kV. EIS measurements were performed on a Gamry Interface 1000 potentiostat/galvanostat/ZRA. For the measurements of EIS, a screen printed electrode (SPE, DropSens) was used and prepared as follows. The photocatalyst sample (10 mg) was dispersed in water (6 mL) and the mixture was homogeneously mixed in an ultrasonic bath for 15 min. The mixture (20 µL) was then dropped onto the working electrode of the SPE, followed by immersion of the SPE in 6 mL of electrolyte which was a mixture of sodium sulfate (0.1 M) and potassium ferricyanide (2.5 mM). The frequency range was set in the range of 1 MHz to 100 mHz. A simplex model program (Gamry Echem Analyst) was selected to fit the obtained Nyquist plot by using constant phase element (CPE) with diffusion as the equivalent circuit model. The emission sites of the samples were investigated using a JASCO FP-8500 spectrofluorometer, in which the excitation wavelength was fixed at 218 nm. The reproducibility for emission spectra measurements was around 4%.

Photocatalytic tests

The photocatalytic activity of the Fe_2O_3/TiO_2 nanocomposites prepared by both photodeposition and impregnation methods was tested for the removal of 2,4-D under irradiation of UV light for 1 h. The photocatalyst (50 mg) was dispersed in a 2,4-D solution (0.5 mM, 50 mL) and stirred for 1 h in the dark to achieve adsorption–desorption equilibrium. The photocatalytic reaction was then conducted under irradiation of a 200 W Hg-Xe lamp (Hamamatsu, light intensity of 8 mW/cm^2 at 365 nm) for 1 h at room temperature. After each reaction, the solution was separated from the photocatalyst by using a membrane filter. The concentration of 2,4-D was determined using a high-performance liquid chromatography instrument (Shimadzu, Prominence LC-20A with Hypersil gold PFP column), which was monitored at a wavelength of 283 nm. The percentage of 2,4-D removal was determined following Equation 3:

$$\text{2,4-D removal}(\%) = \frac{C_o - C_t}{C_o} \times 100\% \quad (3)$$

where C_o is the initial concentration of 2,4-D after reaching adsorption–desorption equilibrium under dark conditions, while C_t is the remaining concentration of 2,4-D after the reaction. Further investigation on the role of active species contributing to the removal of 2,4-D was carried out on the $Fe_2O_3(0.5)/TiO_2$ (PD) nanocomposite, which showed the best photocatalytic activity. Ammonium oxalate, benzoquinone, and *tert*-butanol were used as the various scavengers for photogenerated holes, superoxide radicals and hydroxyl radicals, respectively. The scavenger was introduced to the 2,4-D solution in the presence of the photocatalyst with 1 mole ratio of scavenger/pollutant.

The photostability of the $Fe_2O_3(0.5)/TiO_2$ (PD) nanocomposite was investigated by evaluating the photocatalytic activity for removal of 2,4-D over three cycles. After the first run of reaction under 1 h UV irradiation, the photocatalyst was collected from the 2,4-D solution and was washed with deionised water before drying at 80 °C overnight. The second and third cycles of reactions were conducted using the recovered photocatalyst under similar experimental and treatment conditions, as mentioned above.

Supporting Information

Supporting Information File 1

Additional figures.

The supporting information file contains seven figures with additional experimental data labelled as Figure S1–S7.

[http://www.beilstein-journals.org/bjnano/content/supplementary/2190-4286-8-93-S1.pdf]

Acknowledgements

The research leading to these results has received funding from the European Union Seventh Framework Program (EU-FP7) under the 4G-PHOTOCAT grant (agreement no.: 309636). This work has been also financially supported by the Ministry of Higher Education (MOHE) and Universiti Teknologi Malaysia (UTM, Malaysia) through the international contract matching grant (cost center code: R.J130000.7626.4C035).

References

1. Lazar, M. A.; Varghese, S.; Nair, S. S. *Catalysts* **2012,** *2,* 572–601. doi:10.3390/catal2040572
2. Gupta, M. S.; Triphati, M. *Chin. Sci. Bull.* **2011,** *56,* 1639–1657. doi:10.1007/s11434-011-4476-1
3. Ran, J.; Zhang, J.; Yu, J.; Jaroniec, M.; Qiao, S. Z. *Chem. Soc. Rev.* **2014,** *43,* 7787–7812. doi:10.1039/C3CS60425J
4. Yang, J.; Wang, D.; Han, H.; Li, C. *Acc. Chem. Res.* **2013,** *46,* 1900–1909. doi:10.1021/ar300227e
5. Sun, Q.; Leng, W.; Li, Z.; Xu, Y. *J. Hazard. Mater.* **2012,** *229–230,* 224–232. doi:10.1016/j.jhazmat.2012.05.098
6. Zhao, B.; Mele, G.; Pio, I.; Li, J.; Palmisano, L.; Vasapollo, G. *J. Hazard. Mater.* **2010,** *176,* 569–574. doi:10.1016/j.jhazmat.2009.11.066

7. Ghasemi, S.; Rahimnejad, S.; Setayesh, S. R.; Rohani, S.; Gholami, M. R. *J. Hazard. Mater.* **2009,** *172,* 1573–1578. doi:10.1016/j.jhazmat.2009.08.029
8. Shawabkeh, R. A.; Khashman, O. A.; Bisharat, G. I. *Int. J. Chem.* **2010,** *2,* 10–18. doi:10.5539/ijc.v2n2p10
9. Zhu, J.; Zheng, W.; He, B.; Zhang, J.; Anpo, M. *J. Mol. Catal. A: Chem.* **2004,** *216,* 35–43. doi:10.1016/j.molcata.2004.01.008
10. Xia, Y.; Yin, L. *Phys. Chem. Chem. Phys.* **2013,** *15,* 18627–18634. doi:10.1039/c3cp53178c
11. Li, X.; Lin, H.; Chen, X.; Niu, H.; Liu, J.; Zhang, T.; Qu, F. *Phys. Chem. Chem. Phys.* **2016,** *18,* 9176–9185. doi:10.1039/C5CP06681F
12. Barreca, D.; Carraro, G.; Warwick, M. E. A.; Kaunisto, K.; Gasparotto, A.; Gombac, V.; Sada, C.; Turner, S.; Van Tendeloo, G.; Maccato, C.; Fornasiero, P. *CrystEngComm* **2015,** *17,* 6219–6226. doi:10.1039/C5CE00883B
13. Balbuena, J.; Carraro, G.; Cruz, M.; Gasparotto, A.; Maccato, C.; Pastor, A.; Sada, C.; Barreca, D.; Sánchez, L. *RSC Adv.* **2016,** *6,* 74878–74885. doi:10.1039/C6RA15958C
14. Subramonian, W.; Wu, T. Y.; Chai, S.-P. *J. Environ. Manage.* **2017,** *187,* 298–310. doi:10.1016/j.jenvman.2016.10.024
15. Moniz, S. J. A.; Shevlin, S. A.; An, X.; Guo, Z.-X.; Tang, J. *Chem. – Eur. J.* **2014,** *20,* 15571–15579. doi:10.1002/chem.201403489
16. Litter, M. I.; Navío, J. A. *J. Photochem. Photobiol., A: Chem.* **1994,** *84,* 183–193. doi:10.1016/1010-6030(94)03858-9
17. Di Paola, A.; Marcì, G.; Palmisano, L.; Schiavello, M.; Uosaki, K.; Ikeda, S.; Ohtani, B. *J. Phys. Chem. B* **2002,** *106,* 637–645. doi:10.1021/jp013074l
18. Di Paola, A.; García-López, E.; Ikeda, S.; Marcì, G.; Ohtani, B.; Palmisano, L. *Catal. Today* **2002,** *75,* 87–93. doi:10.1016/S0920-5861(02)00048-2
19. Peña-Flores, J. I.; Palomec-Garfias, A. F.; Márquez-Beltrán, C.; Sánchez-Mora, E.; Gómez-Barojas, E.; Pérez-Rodríguez, F. *Nanoscale Res. Lett.* **2014,** *9,* No. 499. doi:10.1186/1556-276x-9-499
20. Siah, W. R.; Lintang, H. O.; Shamsuddin, M.; Yoshida, H.; Yuliati, L. *Catal. Sci. Technol.* **2016,** *6,* 5079–5087. doi:10.1039/C6CY00074F
21. Siah, W. R.; Lintang, H. O.; Yuliati, L. *Catal. Sci. Technol.* **2017,** *7,* 159–167. doi:10.1039/c6cy01991a
22. Roslan, N. A.; Lintang, H. O.; Yuliati, L. *Adv. Mater. Res.* **2015,** *1112,* 180–183. doi:10.4028/www.scientific.net/AMR.1112.180
23. Burns, C. J.; Swaen, G. M. H. *Crit. Rev. Toxicol.* **2012,** *42,* 768–786. doi:10.3109/10408444.2012.710576
24. El Harmoudi, H.; El Gaini, L.; Daoudi, E.; Rhazi, M.; Boughaleb, Y.; El Mhammedi, M. A.; Migalska-Zalas, A.; Bakasse, M. *Opt. Mater.* **2014,** *36,* 1471–1477. doi:10.1016/j.optmat.2014.03.040
25. Mustafa, Y. A.; Abdul-Hameed, H. M.; Razak, Z. A. *Clean: Soil, Air, Water* **2015,** *43,* 1241–1247. doi:10.1002/clen.201400623
26. Hu, J-y.; Morita, T.; Magara, Y.; Aizawa, T. *Water Res.* **2000,** *34,* 2215–2222. doi:10.1016/S0043-1354(99)00385-1
27. Sun, Y.; Pignatello, J. J. *Environ. Sci. Technol.* **1995,** *29,* 2065–2072. doi:10.1021/es00008a028
28. Djebbar, K.; Zertal, A.; Sehili, T. *Environ. Technol.* **2006,** *27,* 1191–1197. doi:10.1080/09593332708618732
29. Watanabe, N.; Horikoshi, S.; Suzuki, K.; Hidaka, H.; Serpone, N. *New J. Chem.* **2003,** *27,* 836–843. doi:10.1039/b211963n
30. Kim, J.; Choi, W. *Appl. Catal., B: Environ.* **2011,** *106,* 39–45.
31. Siah, W. R.; Lintang, H. O.; Shamsuddin, M.; Yuliati, L. *IOP Conf. Ser.: Mater. Sci. Eng.* **2016,** *107,* 012005. doi:10.1088/1757-899x/107/1/012005
32. Yuliati, L.; Siah, W. R.; Roslan, N. A.; Shamsuddin, M.; Lintang, H. O. *Malaysian J. Anal. Sci.* **2016,** *20,* 171–178. doi:10.17576/mjas-2016-2001-18
33. Pendlebury, S. R.; Wang, X.; Le Formal, F.; Cornuz, M.; Kafizas, A.; Tilley, S. D.; Grätzel, M.; Durrant, J. R. *J. Am. Chem. Soc.* **2014,** *136,* 9854–9857. doi:10.1021/ja504473e
34. Valencia, S.; Marín, J. M.; Restrepo, G. *Open Mater. Sci. J.* **2009,** *4,* 9–14. doi:10.2174/1874088x01004010009
35. Tian, G.; Fu, H.; Jing, L.; Xin, B.; Pan, K. *J. Phys. Chem. C* **2008,** *112,* 3083–3089. doi:10.1021/jp710283p
36. Devi, L. G.; Murthy, B. N.; Kumar, S. G. *Mater. Sci. Eng., B* **2010,** *166,* 1–6. doi:10.1016/j.mseb.2009.09.008
37. Khan, M. M.; Ansari, S. A.; Pradhan, D.; Ansari, M. O.; Han, D. H.; Lee, J.; Cho, M. H. *J. Mater. Chem. A* **2014,** *2,* 637–644. doi:10.1039/C3TA14052K
38. Nkosi, D.; Pillay, J.; Ozoemena, K. I.; Nouneh, K.; Oyama, M. *Phys. Chem. Chem. Phys.* **2010,** *12,* 604–613. doi:10.1039/B918754E
39. Cong, Y.; Zhang, J.; Chen, F.; Anpo, M. *J. Phys. Chem. C* **2007,** *111,* 6976–6982. doi:10.1021/jp0685030
40. Yang, M.-Q.; Zhang, Y.; Zhang, N.; Tang, Z.-R.; Xu, Y.-J. *Sci. Rep.* **2013,** *3,* 3314. doi:10.1038/srep03314
41. Munter, R. *Proc. Est. Acad. Sci., Chem.* **2001,** *50,* 59–80.
42. Trillas, M.; Peral, J.; Domènech, X. *Appl. Catal., B: Environ.* **1993,** *3,* 45–53. doi:10.1016/0926-3373(93)80067-N
43. Xu, Y.; Schoonen, M. A. A. *Am. Mineral.* **2000,** *85,* 543–556. doi:10.2138/am-2000-0416

License and Terms